Magma ascent mechanisms in the transition regime from solitary porosity waves to diapirism

Janik Dohmen[1], Harro Schmeling[1]

[1]Institute for Geoscience, Goethe University, Frankfurt, Germany

Correspondence to: dohmen@geophysik.uni-frankfurt.de

Abstract

In partially molten regions inside the earth melt buoyancy may trigger upwelling of both solid and fluid phases, i.e. diapirism. If the melt is allowed to move separately with respect to the matrix, melt perturbations may evolve into solitary porosity waves. While diapirs may form on a wide range of scales, porosity waves are restricted to sizes of a few times the compaction length. Thus, the size of a partially molten perturbation controls whether a diapir or a porosity wave will emerge. We study the transition from diapiric rise to solitary porosity waves by solving the two-phase flow equations of conservation of mass and momentum in 2D with porosity dependent matrix viscosity. We systematically vary the initial size of a porosity perturbation from 1.5 to 100 times the compaction length. If the perturbation is much larger than a regular solitary wave, its Stokes velocity is large and therefore faster than the segregating melt. Consequently, the fluid is not able to form a porosity wave and a diapir emerges. For small perturbations solitary waves emerge, either with a positive or negative vertical matrix velocity inside. In between the diapir and solitary wave regimes we observe a third regime of porosity wave or diapir induced melt focusing and channeling. In these cases, diapirism is dominant but the fluid is still fast enough to locally build up channels and rise in front of the bigger perturbation. These channels have a scale of the order of a few compaction lengths and evolve as long as this length scale is decently resolved. We assume, based on resolution tests, that channels will also build up in the diapir regime with higher resolution.

1 Introduction

In many scenarios inside the earth the process of a fluid moving relatively to a viscously deformable porous matrix is an important transport mechanism. The physics of these scenarios were firstly described by McKenzie (1984) and it was later shown by several authors that these equations allow for the emergence of solitary porosity waves (Scott & Stevenson, 1984; Barcilon & Lovera 1989; Wiggins & Spiegelman, 1995). Porosity waves are regions of localized excess fluid that ascend with permanent shape and constant velocity, controlled by compaction and decompaction of the surrounding matrix.

Even though these porosity waves were of vast interest for many authors over the last decades and the possible consequences on geochemistry and fluid flow in lower and middle crust in general (e.g. Watson & Spiegelman, 1994; McKenzie, 1984; Connolly, 1997; Connolly & Podladchikov, 2013, Jordan et al., 2018, Richard et al., 2012) or the effects of matrix rheology on porosity waves (e.g. Connolly & Podladchikov, 1998; Yarushina et al., 2015; Connolly & Podladchikov, 2015; Omlin et al., 2017;

Dohmen et al., 2019) have been examined, there are still open questions. One open question is that of the scaling. The size of a solitary porosity wave is usually of the order of a few compaction lengths (McKenzie, 1984; Scott & Stevenson, 1984; Simpson & Spiegelman, 2011), but this length scale varies over a few orders of magnitude, depending on the shear and bulk viscosity of the matrix, fluid viscosity and permeability (see 1) with typical values of 100-10000 meters (McKenzie, 1984; Spiegelman, 1993).

On the other hand, partially molten regions in the lower crust or upper mantle are prone to gravitational instabilities such as Rayleigh-Taylor instabilities or diapirism (e.g. Griffith, 1986; Bittner and Schmeling, 1995; Schmeling et al., 2019). As characteristic wavelengths of Rayleigh-Taylor instabilities may be similar, but also of significantly different order of those of porosity waves, the question arises how these two mechanisms interact and how does the transition between magmatic rise due to diapirism or porosity wave look like. Scott (1988) already had a look at a similar scenario. He calculated porosity waves changing the compaction length by altering the shear to bulk viscosity ratio, while we want to change the radius of a partially molten perturbation in terms of compaction lengths but keeping the viscosity the same. While Scott (1988) was not able to reach the single-phase flow endmember due to his setup we can reach this endmember with our description and can show how the transition looks like.

The extent of partially molten scenarios inside the earth's mantle vary over many orders of magnitude and this transition might have an important effect on the evolution of these regions. In this work we want to address this problem and look especially on what happens for different sizes of initial perturbations and what are the numerical implications on modelling magma transport.

Addressing different melt ascent mechanisms, it may be useful to specify our definition of diapirism. Originating from the Greek "*diapeirein"*, i.e. "to pierce through", diapirism describes the "buoyant upwelling of relatively light rock" (Turcotte & Schubert, 1982) through and into a denser overburden. In the general definition the rheology of the diapir and ambient material is not specified, both can be ductile as in our case, but often, the overburden is assumed being more viscous or even brittle. Buoyancy may be of compositional or phase related origin, e.g. due to the presence of non-segregating partial melt (Wilson, 1989). Based on these definitions in our case a diapir is a rising, partially molten body or porosity anomaly with zero fluid-solid separation velocity. Mathematically the equations of motion of the two-phase system degenerate to the Stokes equation (see below).

2 Theoretical Approach

2.1 Governing equations

The formulation of the governing equations for the melt-in-solid two-phase flow dynamics is based on McKenzie (1984), Spiegelman & McKenzie (1987) and Schmeling (2000) assuming an infinite Prandtl number, a low fluid viscosity w.r.t. the effective matrix viscosity, zero surface tension, and the Boussinesq approximation. In the present formulation the Boussinesq approximation (BA) assumes the same constant density for the solid and fluid except for the buoyancy terms of the momentum equations

for the solid and fluid. In the following all variables associated with the fluid (melt) have the subscript f and those associated with the solid have the subscript s. Applying the BA the equation for the conservation of the mass of the melt is

$$\frac{\partial \varphi}{\partial t} + \vec{\nabla} \cdot \left(\varphi \vec{v}_f\right) = 0, \tag{1}$$

and the mass conservation of the solid is

$$\frac{\partial (1-\varphi)}{\partial t} + \vec{\nabla} \cdot ((1-\varphi)\vec{v}_s) = 0. \tag{2}$$

φ is the volumetric rock porosity (often called melt fraction), $\vec{v}_f$ and $\vec{v}_s$ are the fluid and solid velocities, respectively. The momentum equations are given as a generalized Darcy equation for the fluid separation flow

$$\vec{v}_f - \vec{v}_s = -\frac{k_\varphi}{\eta_f \varphi}\left(\vec{\nabla} P - \rho_f \vec{g}\right), \tag{3}$$

where ρ_f is the fluid density, and the Stokes equation for the mixture

$$\rho \vec{g} - \vec{\nabla} P + \frac{\partial \tau_{ij}}{\partial x_j} = 0. \tag{4}$$

k_φ is the permeability that depends on the rock porosity

$$k_\varphi = k_0 \varphi^n, \tag{5}$$

η_f is the melt dynamic viscosity, $\vec{g}$ is the gravitational acceleration, ρ is the density of the melt – solid mixture, P is the fluid pressure (including the lithostatic pressure), whose gradient is driving the motion, and τ_{ij} is the viscous stress tensor

$$\tau_{ij} = \eta_s \left(\frac{\partial v_{si}}{\partial x_j} + \frac{\partial v_{sj}}{\partial x_i}\right) + \left(\eta_b - \frac{2}{3}\eta_s\right) \delta_{ij} \nabla \cdot \vec{v}_s. \tag{6}$$

η_b is the bulk viscosity. The linearized equation of state for the mixture density is given as

$$\rho = \rho_0 \left(1 - c_f \varphi\right) \tag{7}$$

with ρ_0 as the solid density and $c_f = \frac{\rho_0 - \rho_f}{\rho_0}$. The shear and bulk viscosity are given by the simple equations

$$\eta_s = \eta_{s0}(1-\varphi) \tag{8}$$

and

$$\eta_b = \eta_{s0} \frac{1-\varphi}{\varphi} \tag{9}$$

where η_{s0} is the intrinsic shear viscosity of the matrix.

As in both equations (3) and (4) P is the fluid pressure, these equations can be merged to eliminate the pressure resulting in

$$\vec{v}_f - \vec{v}_s = -\frac{k_0 \varphi^{n-1}}{\eta_f}\left(\rho_0 c_f \vec{g}(1-\varphi) + \frac{\partial \tau_{ij}}{\partial x_j}\right). \quad (10)$$

This equations states that the fluid separation flow i.e. melt segregation velocity) is driven by the buoyancy of the fluid with respect to the solid and the viscous stress in the matrix including compaction and decompaction.

Following Šrámek *et al.* (2007) the Stokes equation (3) can be rewritten by expressing the matrix velocity, $\vec{v}_s$, as the sum of the incompressible flow velocity, $\vec{v}_1$, and the irrotational (compaction) flow velocity, $\vec{v}_2$, as:

$$\vec{v}_s = \vec{v}_1 + \vec{v}_2 = \begin{pmatrix} \frac{\partial \psi}{\partial z} \\ -\frac{\partial \psi}{\partial x} \end{pmatrix} + \begin{pmatrix} \frac{\partial \chi}{\partial x} \\ \frac{\partial \chi}{\partial z} \end{pmatrix} \quad (11)$$

with ψ as stream function and χ as the irrotational velocity potential, given as the solution of the Poisson equation

$$\vec{\nabla}^2 \chi = \vec{\nabla} \cdot \vec{v}_s. \quad (12)$$

The divergence term $\vec{\nabla} \cdot \vec{v_s}$ can be derived from eqs. 1 and 2 to give

$$\vec{\nabla} \cdot \vec{v}_s = -\vec{\nabla} \cdot \left[\varphi(\vec{v}_f - \vec{v}_s)\right]. \quad (13)$$

In the small fluid viscosity limit the viscous stresses within the fluid phase are neglected, resulting in a viscous stress tensor in the Stokes equation of the mixture (equ. 4), in which only the stresses in the solid phase are relevant. This is evident from the definition of the viscous stress tensor, which only contains matrix and not fluid viscosities. Melt viscosities of carbonatitic, basaltic or silicic wet or dry melts span a range from < 1 Pa s to extreme values up to 10^{14} Pa s (see the discussion in Schmeling et al., 2019), while effective viscosities of mafic or silicic partially molten rocks may range between 10^{20} Pa s and 10^{16} Pa s, depending on melt fraction, stress, and composition. Thus, in most circumstances the small fluid viscosity limit is justified.

In the limit of this small viscosity assumption, inserting the above solid velocity (11) into the viscous stress (6), this into the Stokes equation (4), and taking the curl of the x- and z equations the pressure is eliminated and one gets

$$\left(\frac{\partial^2}{\partial x^2} - \frac{\partial^2}{\partial z^2}\right)\left[\eta_s\left(\frac{\partial^2 \psi}{\partial x^2} - \frac{\partial^2 \psi}{\partial z^2}\right)\right] + 4\frac{\partial^2}{\partial x \partial z}\left[\eta_s \frac{\partial^2 \psi}{\partial x \partial z}\right] = -g\frac{\partial \rho}{\partial x} + A(\chi) \quad (14)$$

with

$$A(\chi) = -2\frac{\partial^2}{\partial x \partial z}\left[\eta_s\left(\frac{\partial^2 \chi}{\partial x^2} - \frac{\partial^2 \chi}{\partial z^2}\right)\right] + 2\left(\frac{\partial^2}{\partial x^2} - \frac{\partial^2}{\partial z^2}\right)\left[\eta_s \frac{\partial^2 \chi}{\partial x \partial z}\right] \quad (14a)$$

To describe the transition from solitary waves to diapirs it is useful to non-dimensionalize the equations. As scaling quantities we use the radius r of the anomaly, the reference viscosity η_0, and the scaling Stokes sphere velocity (e.g. Turcotte & Schubert, 1982) based on the maximum porosity of the porosity anomaly φ_{max}

$$v_{St} = \frac{\varphi_{max} \Delta\rho g r^2}{\eta_0} \quad (15)$$

resulting to the following non-dimensionalization where non-dimensional quantities are primed:

$$(x, z) = (x', z') \cdot r\,, \qquad \vec{v}_{s,f} = \vec{v}_{s,f}{}' \cdot v_{St}, \qquad t = t' \cdot \frac{r}{v_{St}}, \qquad (\tau_{ij}, P) = (\tau_{ij}{}', P') \cdot \frac{\eta_0 v_{St}}{r},$$

$$(\eta_s, \eta_b) = (\eta_s{}', \eta_b{}') \cdot \eta_0, \qquad (\psi, \chi) = (\psi', \chi') \cdot r v_{St} \quad (16)$$

We use the width corresponding to a $1/e$ drop of the initial perturbation as radius for the Stokes velocity. This is reasonable as the amount of melt in the perturbation is approximately equal to the amount of melt in a spheres cut with a sharp boundary of radius r, for what the Stokes equation is valid.

With these rules the Darcy equation (10) is given in non-dimensional form

$$\vec{v}_f{}' - \vec{v}_s{}' = -\frac{\varphi^{n-1}}{Rt}\left(\vec{e}_z \frac{(1-\varphi)}{\varphi_{max}} + \frac{\partial \tau_{ij}'}{\partial x_j'}\right) \quad (17)$$

where

$$Rt = \frac{\eta_f r^2}{\eta_0 k_0} \quad (18)$$

is the retention number based on the length scale of the anomaly and $\vec{e}_z$ is the unit vector in z-direction, and the momentum equation of the mixture (12) is given by

$$\left(\frac{\partial^2}{\partial x'^2} - \frac{\partial^2}{\partial z'^2}\right)\left[\eta_s{}'\left(\frac{\partial^2 \psi'}{\partial x'^2} - \frac{\partial^2 \psi'}{\partial z'^2}\right)\right] + 4\frac{\partial^2}{\partial x' \partial z'}\left[\eta_s{}' \frac{\partial^2 \psi'}{\partial x' \partial z'}\right] = \frac{1}{\varphi_{max}}\frac{\partial \varphi}{\partial x'} + A'(\chi') \quad (19)$$

In the other equations (1), (2), (6), (11), (12), (13), and (14a) all quantities are simply replaced by their non-dimensional primed equivalents.

We now can compare the two limits, where segregation or two-phase flow dominates (solitary wave regime), and where fluid and solid rise together with the same velocity as partially molten bodies (batch melting), which we identify with the diapir regime. This can be done by comparing the characteristic segregation velocity within solitary waves, which scales as

$$v_{sgr} \approx \frac{k_0 {\varphi_{max}}^{n-1}}{\eta_f}\left(\Delta\rho g(1-\varphi_{max}) - \frac{\partial \tau_{ij}}{\partial x_j}\right) = C\frac{k_0 {\varphi_{max}}^{n-1} \Delta\rho g(1-\varphi_{max})}{\eta_f} \quad (20)$$

where C is of the order ½ for 2D solitary waves (Schmeling, 2000), with the characteristic Stokes sphere rising velocity given by (15). The ratio of these is given by

$$\frac{v_{sgr}}{v_{st}} = C\frac{{\varphi_{max}}^{n-2}(1-\varphi_{max})}{Rt} \tag{21}$$

Thus, *in the solitary wave limit*

$$\frac{Rt}{C{\varphi_{max}}^{n-2}(1-\varphi_{max})} \ll 1 \tag{22}$$

and Darcy's law (17) results in large segregation velocity, which scales as

$${v_{sgr}}' = C\frac{(1-\varphi_{max}){\varphi_{max}}^{n-1}}{Rt} \tag{23}$$

From equation (13) it follows that the irrotational part of the matrix velocity scales with

$$v_1 \approx -\varphi_{max} v_{sgr} \tag{24}$$

while the rotational part is given by (19): In that equation A' scales with χ', which, via equ (12) and (13), scale with v_{sgr}, i.e. with $\frac{1}{Rt}$. In other words, the second term on the RHS of (19) dominates for small Rt as the first term is of the order 1. Thus, the rotational matrix velocity has the same order as the irrotational compaction velocity and serves to accommodate the compaction flow. In this limit the buoyancy term in equation (19), $\frac{1}{\varphi_{max}}\frac{\partial\varphi}{\partial x\prime}$, is of vanishing importance for the matrix velocity and the matrix velocity, $\vec{v}_1 + \vec{v}_2$, is of the order of $\varphi_{max} v_{sgr}$. In the small porosity limit, matrix velocities are negligible with respect to fluid velocities.

In the diapir limit,

$$\frac{Rt}{C{\varphi_{max}}^{n-2}(1-\varphi_{max})} \gg 1 \tag{25}$$

and equation (17) predict vanishing segregation velocities. As A' and χ' scale with $\frac{1}{Rt}$, both vanish in the diapir limit, no irrotational matrix velocity occurs and equ. (19) reduces to the classical biharmonic equation (i.e. Stokes equation) driven by melt buoyancy. Segregation velocities are negligible with respect to matrix velocities.

We will often refer to the compaction length, δ_c, which is a typical length scale used in two-phase flow problems (McKenzie, 1984). Of particular importance in our context, 2D porosity waves have half widths radii of the order of $3\delta_c$ to $5\delta_c$ (Simpson and Spiegelman, 2011). The compaction length is defined as:

$$\delta_c = \sqrt{\frac{\eta_b + \frac{4}{3}\eta_s}{\eta_f} k_\varphi} \tag{26}$$

The non-dimensional value $\delta_c' = \frac{\delta_c}{r}$ can be calculated using Rt with

$$\delta_c' = \sqrt{\frac{\eta_b' + \frac{4}{3}\eta_s'}{Rt} \varphi^n} \tag{27}$$

2.2 Model setup

The model consists of a $L' \times L'$ box with a background porosity, φ_0, of 0.5%. L' is the the non-dimensional side length of the box and equal to 20 times the initial radius of the perturbation. As initial condition a non-dimensional Gaussian wave porosity anomaly is placed at ${x_0}' = 10$ and ${z_0}' = 4$. It has the form of

$$\varphi = A \cdot \exp\left(-\left(\frac{x' - {x_0}'}{r'}\right)^2 - \left(\frac{z' - {z_0}'}{r'}\right)^2\right) \tag{28}$$

where A is the amplitude equal to 0.03 in our models and r' the non-dimensional width of the wave. r' in the model is always equal to 1, as it is used for non-dimensionalization. To vary the radius of the anomaly in terms of compaction lengths we change the retention number, which varies the compaction length. While the radius of an emerging solitary wave is always in the order of a few compaction lengths, by varying Rt, the radius of the initial anomaly is varied between 1.5 and 100 times the compaction length to explore the parameter range in which diapirs might become dominant. The model box has always the same resolution, but the compaction length is differently resolved for each model. Even though this might lead to problems, as the compaction length should be always resolved equally, we are not able to do this, because our model series will inevitably lead to very small compaction lengths and keeping it equally resolved would require model resolutions we are not capable of performing. The numerical issues regarding this will be addressed later in this work.

At the top and the bottom, we prescribe an out- and inflow for both melt and solid, respectively, which is calculated analytically for the background porosity. This is necessary because we have a background melt fraction φ_0, that has a certain buoyancy which would lead to an accumulation of melt at the top of the model. We therefore calculate the segregation velocity of the background porosity φ_0 using equation (17) without the viscous stress term. The corresponding matrix velocity is calculated using the conservation of mass.

At the sides we use mirroring boundary conditions, which corresponds to a symmetry axis, where no horizontal flow is allowed. The permeability-porosity relation exponent in our models is always $n = 3$.

Our strategy is to vary the width of the initial porosity wave to cover the range from solitary waves to diapiric rise. Practically this is done by varying Rt and keep the non-dimensional radius constant. Here we give a small example:

For $Rt = 10^{-4}$ the initial perturbation, which has always a non-dimensional radius of $r' = 1$, has a dimensional radius of $r = 1.5 \cdot \delta_c$. With $Rt = 2.5 \cdot 10^{-3}$, the dimensional radius will be equal to $r = 10 \cdot \delta_c$, while r' is still equal to 1. Suppositious a solitary wave has always a similar radius in terms of compaction lengths, in the first case a solitary wave with $r_{sw} = 5 \cdot \delta_c$ will in our non-dimensionalization have a radius of $r'_{sw} = 2.5$. While in the second case the same wave will have a radius of $r'_{sw} = 0.5$. In a dimensional world this might correspond to enlarging the initial perturbation and keeping the compaction length constant or vice versa.

2.3 Numerical strategy

The above equations in non-dimensional form are solved by the finite differences code FDCON developed essentially by one of the authors (Schmeling). In the following, the non-dimensional versions of all equations are used. Starting from the prescribed initial condition for φ, and assuming $A'(\chi') = 0$ at time 0, the time loop is entered and the biharmonic equation (19) is solved for ψ' by Cholesky decomposition, from which $\vec{v}_1{}'$ is derived. Together with $\vec{v}_2{}'$ the resulting solid velocity is used to determine the viscous stress term in the segregation velocity equation (17). This equation and the melt mass equation (1) are solved iteratively with strong damping for φ and $\vec{v}_f{}' - \vec{v}_s{}'$ for the new time step using upwind and an implicit formulation of equ. (1). During this internal iteration these quantities are used, via equ. (13), to give $\vec{\nabla} \cdot \vec{v}_s$, the divergence of the matrix velocity, which is needed in the viscous stress term (equ. 6). After convergence $\vec{\nabla} \cdot \vec{v}_s$ is used via equ. (12) to determine χ by LU-decomposition and then to get $\vec{v}_2{}'$. Now $A'(\chi')$ can be determined to be used on the RHS of equ (19). The procedure is then repeated upon entering the next time step.

Time steps are dynamically adjusted by the Courant criterion times 0.2 based on the fastest velocity, either melt or solid. We use a regular grid with 201 x 201 grid points.

3 Results

3.1 The transition from porosity wave to diapirism: Varying the initial wave radius

In this model series we vary the initial wave radius to cover the transition from porosity waves to diapirs. For small radii ($r \leq 10 \cdot \delta_c$) we can clearly see the emergence of solitary waves (Fig. 1 top row). $r = 1.5 \cdot \delta_c$ leads to a wave that is nearly the size of the initial perturbation. Even smaller radii would lead to bigger waves but with a smaller porosity amplitude as the melt needs to be conserved. For bigger radii the resulting solitary waves become smaller with respect to the initial size and lead to a focusing of melt. With an initial radius of $10 \cdot \delta_c$ the resulting wave has just a size of ~20% the initial wave size after it has risen half a box length.

We can compare the observed rising velocities of these solitary waves of Fig. 1 a to d with hypothetical Stokes velocities of an equivalent diapir based on equ. (15). While the dimensional Stokes velocity of a porosity anomaly is proportional to the amplitude of porosity and the square of the radius, the non-dimensional Stokes velocity is always equal to 1. In Fig. 2 this non-dimensional Stokes velocity is indicated by the dashed line with the value 1. The colored lines in Fig. 2 give 2D solitary wave velocities, given by Simpson & Spieglman (2011), normalized by the Stokes velocity corresponding to different initial perturbation radii. Inspection of Fig. 2 reveals that for the first 4 cases of Fig. 1a to d with radii smaller or equal $10 \cdot \delta_c$ the phase velocities are always larger than the Stokes velocity, i.e. the cases are in the solitary wave regime.

For greater radii (e.g. $r = 20 \cdot \delta_c$ or $30 \cdot \delta_c$, Fig. 1e or f, respectively) we see a focusing of melt in a narrow channel with a width of a few grid sizes. Inspection of Fig. 2 reveals that the solitary wave phase velocity of these cases is smaller than the Stokes velocity of the total porosity anomaly. We expect that the Stokes velocity of the non-circular porosity anomaly at later stages such as the stages shown in Fig. 1 is still of the order of the circular anomaly which approximately obeys equ. (15). Thus, the observed channel is no more the wake of a very small leading porosity wave, which is no more properly resolved by the numerical grid. Instead, we conjecture that these cases represent the transition to diapiric rise of the porosity anomaly, during which horizontal extensive stresses and strain rates within the upper, frontal part of the diapir lead to a channeling instability. Such channeling instabilities have been predicted in 1D by Stevenson (1989) and have been modelled without buoyancy by Richardson (1998) in 2D. Golabek et al. (2008) obtained such channels in a partially molten mantle in front of sinking dense bodies. The channels were oriented radially away from the frontal hemisphere of the body, with the dominating channel pointing in the direction of the movement of the dense body. According to Stevenson (1989) the characteristic wavelength of such channels is expected to be of the order of $2\pi\delta_c$. In Fig. 1e and f the width of the observed channels is about $6 - 9 \cdot \delta_c$, i.e. on the order of the characteristic wavelength. With a grid size of $2 \cdot \delta_c$ and $3 \cdot \delta_c$ for the cases shown in Fig. 1e and f the channels are close to but still above the resolution limit. In contrast to Golabek et al. (2008) the leading channel immediately dominates and is fed by buoyant melt out of the following porosity anomaly, no side channels evolve as in Golabek et al., (2008). This is probably due to their different compositional approach which prohibits such feeding. This channeling instability will be further discussed below.

For $r > 40 \cdot \delta_c$ the channeling instability disappears, probably because it is below the resolution limit (grid size $< 4 \cdot \delta_c$ for $r > 40 \cdot \delta_c$) and we enter the diapir regime. In the diapir regime all perturbations evolve similar with a comparable velocity and in the same shape. In this diapir regime ($r > 40 \cdot \delta_c$) Fig. 2 shows that the solitary wave velocities are at least one order of magnitude below the Stokes velocity of the diapir.

Summarizing Fig. 2, the comparison of Stokes and porosity wave velocities correlates nicely with the transition from diapirism to solitary waves shown in Fig. 1: For bigger radii the Stokes velocities are

higher than the solitary wave velocity and the latter is therefore not the driving force of the ascending process and consequently not able to build up. For small radii the solitary wave velocity is clearly higher and therefore able to build up. Just by comparison of these curves, perturbations with $r > 20 \cdot \delta_c$ should lead to diapirism while $r < 20 \cdot \delta_c$ should lead to solitary waves.

3.2 Effects on the mass flux

It is important to study the partitioning between rising melt and solid mass fluxes in partially molten magmatic systems, because melts and solids are carriers of different chemical components. Within our Boussinesq approximation we may neglect the density differences between solid and melt. Then our models allow to evaluate vertical mass fluxes of solid or fluid by depicting the vertical velocity components multiplied with the melt or solid fractions, respectively:

$$q'_{sz} = (1-\varphi) \cdot v'_{sz}$$
$$q'_{fz} = \varphi \cdot v'_{fz}. \quad (29)$$

Fig. 3 shows horizontal profiles through rising melt bodies at the vertical positions of maximum melt fraction.

The mass fluxes of solid and fluid are strongly affected by the change of the initial radius from the solitary wave regime to the diapiric regime. For $r = 1.5 \cdot \delta_c$, where we observe a solitary wave, the fluid has its peak mass flux in the middle of the wave and the solid is going downwards, against the phase velocity. In the center the fluid flux is more than 10 times higher than the solid. The net upward flow in the center is balanced by the matrix dominated downward flow outside the wave. For $r = 10 \cdot \delta_c$ the wave area is much smaller and the ratio between solid and fluid flux is around the order of one. Even though we observe a local minimum in the center of the wave for the solid flux it is not negative. However, the solid matrix around the wave is affected in a much greater area and, contrary to the case for $r = 1.5 \cdot \delta_c$, the rising net mass flux in and around the melt anomaly is dominated by the solid rather than melt flux.

For $r = 50 \cdot \delta_c$ and $r = 100 \cdot \delta_c$ the solid flux is significantly higher than the fluid flux also within the melt anomaly.

So far, we have based our discussion of the transition between solitary waves and diapirs on qualitative model observations. We now try to invoke a more quantitative criterion. In a horizontal line passing through the anomalies porosity maximum we define the total vertical mass flux of the rising magma body by $\int_{\varphi>\varphi_0}(q_f + q_s)dx$ where the integration is carried out only in the region of increased porosity $\varphi > \varphi_0$. This mass flux is partitioned between the fluid mass flux, $\int_{\varphi>\varphi_0} q_f dx$, and the solid mass flux, $\int_{\varphi>\varphi_0} q_s dx$. With these we define the partition coefficients

$$C_{soli} = \frac{\int_{\varphi>\varphi_0} q_f dx}{\int_{\varphi>\varphi_0} (q_f + q_s) dx} \quad (30)$$

and

$$C_{dia} = \frac{\int_{\varphi>\varphi_0} q_s dx}{\int_{\varphi>\varphi_0} (q_f + q_s) dx} \quad (31)$$

The sum $C_{soli} + C_{dia}$ is always 1 and if $C_{soli} > C_{dia}$ then the solitary wave proportion is dominant, while for $C_{soli} < C_{dia}$ diapirism is dominant. In Fig. 4a these partition coefficients for several initial radii are shown. In red are the partition coefficients calculated at a horizontal line at the height of maximum melt fraction. The blue markers are calculated for horizontal lines at all grid points below the maximum melt fraction as long as $\varphi \geq \frac{\varphi_{max}}{2}$. For $r = 1.5 \cdot \delta_c$, C_{soli} is equal to 1.5 and C_{dia} is equal to -0.5, i.e. we have a downward solid flux. With increasing radius C_{dia} increases until it changes its direction at $r = 4 \cdot \delta_c$. For even bigger radii C_{dia} increases further until it approaches 1 at approximately $r = 40 \cdot \delta_c$. C_{soli} changes so that the sum of both is always equal to 1. Even though diapirism is dominant for $r > 7.5 \cdot \delta_c$ we still observe a small solitary wave for $r = 10 \cdot \delta_c$ (c.f. Fig. 1) and the formation of channels until $r = 40 \cdot \delta_c$ where the melt segregation velocity $\overrightarrow{v_f}$ becomes slower than the matrix velocity $\overrightarrow{v_s}$. In Fig. 4b the ratio of maximum fluid velocity (i.e. $\overrightarrow{v_f}$) to absolute matrix velocity is shown. For small radii, where $C_{soli} \gg C_{dia}$, this ratio is approximately constant with a high value of about 300. The absolute velocity maxima itself are not constant but decrease with the same rate until the switch of negative to positive matrix mass flux, where the absolute matrix velocity starts to increase, while the fluid velocity keeps decreasing. At this zero crossing we would expect a ratio of infinity, but with our models we are far enough away to not see this in the data. This switch from negative to positive mass flux was already observed by Scott (1988), but while he changed the viscosity ratio, we change the radius and keep the viscosity ratio constant. Both describe the transition from a two-phase limit towards the Stokes limit, but in our formulation, we are able to reach the Stokes limit while Scott (1988) is still in the two-phase flow regime. In the regime where a channel forms near the front of the porosity anomaly ($r = 20 \cdot \delta_c$ to $r = 40 \cdot \delta_c$) the ratio decreased from 20 to 2 (i.e. to $\overrightarrow{v_f} = \overrightarrow{v_s}$). In this regime, porous flow within the evolving channels is still very effective, and strongly exceeds the diapiric rising velocity. Above this point the channeling instability is no longer observed and clear diapirism can be observed. The calculated partition coefficients at lower elevations show that within the point of maximum melt fraction, C_{soli} is highest and decreases behind the ascending peak. Apparently, the fluid is locally able to build up a high porosity channel with segregating melt even though diapirism is dominant in the whole region. For small radii the partition coefficients vary strongest because the melt fraction decreases strongly behind the center of the wave.

Based on these observations the evolution of these models can be divided into 3 regimes: (1) In the solitary wave regime ($r \leq 7.5 \cdot \delta_c$) C_{soli} is larger than C_{dia} and the initial perturbation emerges into waves that have the properties of solitary waves and ascend with constant velocity and staying in shape. This regime can be further divided into 1a ($r < 4 \cdot \delta_c$) ,where the solid mass flux is negative, and 1b ($4 \cdot \delta_c < r \leq 7.5 \cdot \delta_c$), where the solid moves upwards with the melt. Waves in these regimes are very similar and differ only in the matrix flux.

In the transitional regime (2) ($7.5 \cdot \delta_c > r \geq 40 \cdot \delta_c$) C_{dia} is bigger than C_{soli} but either a small solitary wave may form near the front of a diapir ($r = 10 \cdot \delta_c$) or diapirs with leading high porosity channels can be observed. Even though diapiric ascend is dominant, melt is locally able to focus into channels because the fluid is still faster than the matrix. This leads to a small peak of high porosity at the front of the channel followed by a broader area ascending as diapir. We may call this regime "porosity wave or diapir induced melt focusing and channeling".

In regime (3) ($r > 40 \cdot \delta_c$) the segregation velocity is smaller than the matrix velocity (i.e. $\frac{\max(v_f)}{\max(v_s)} \leq 2$) and the fluid is therefore no longer able to separate fast enough to build up a solitary wave or a focusing channel. Dominated by solid mass flux a well-developed diapir will ascend.

3.3 Numerical Issues

In Fig. 5 a model with an initial perturbation radius of $r = 60 \cdot \delta_c$ is shown in three different model resolutions. While for the lowest resolution (Fig. 5a) a diapir can be observed, an increased resolution of 301x301 shows some localization of melt at the top of the diapir. With the highest resolution the grid size is equal to approximately two times the compaction length, and a strongly focused channel in front of the initial perturbation builds up, and two weak side lobes appear at a distance of about $28 \cdot \delta_c$ on each side of the channel. Inspecting the wavelength dependence of channeling instabilities (Stevenson, 1989), this is about four times the wavelength at which the growth curve approaches its maximum value and remains constant for smaller wavelengths. Richardson (1998) investigated the melt channeling instability and found that it is grid space dependent: "when the grid spacing is of the order of the compaction length", as in our case in Fig. 5c, "the instability locks onto a small multiple of the grid spacing, and so the solution is affected by the discretization for the numerical calculation" In the cases of Fig. 5a and b the grid spacing is larger than the compaction length prohibiting the evolution of the channeling instability, while in case of Fig. 5c Richardson's (1998) criterion is met and channeling occurs.

With this perception it is interesting to reevaluate the model series in Fig. 1. The models within the diapir-regime and $r > 40 \cdot \delta_c$ do not show any sign of developing a frontal channel. This may be explained by the coarse resolution, because the compaction lengths are significantly less than the grid size. We expect, that if the grid resolution would be increased appropriately as in the resolution test in

Fig. (5), also these models would show frontal channel(s) on the scale of small multiple of the grid spacing. Because of practical reasons we did not test this conjecture for other r's than that in Fig. 5.

4 Discussion

4.1 The channeling instability

In this chapter we compare the observed formation of channels at the top of some of the porosity anomalies with the growth rate of the channeling instability analytically derived by Stevenson (1989). For wavelengths of the order of $2\pi\delta_c$ and smaller the growth rate of channel like porosity perturbations oriented perpendicular to the direction of a background extensional strain rate $\dot{e}_0$ is given by

$$\alpha_0 = \frac{2\eta_s a_\eta \dot{e}_0}{\left(\eta_b + \frac{4}{3}\eta_s\right)} \tag{32}$$

where a_η gives the porosity dependence of the shear viscosity

$$a_\eta = -\frac{d\ln(\eta_s)}{d\varphi} \tag{33}$$

Using our rheology laws (8) and (9) we arrive at

$$\alpha_0 = \frac{2\varphi\dot{e}_0}{(1-\varphi^2)} \tag{34}$$

We non-dimensionalize the growth rate by using our scaling velocity and scaling length, i.e. $\frac{v_{St}}{r}$. This quantity happens to scale with the characteristic strain rate near the top of the circular porosity wave, i.e. with $\dot{e}_0$. Thus, the non-dimensional channeling growth rate reduces to

$$\alpha_0{}' = \frac{2\varphi}{(1-\varphi^2)} \tag{35}$$

Inspecting the time-dependence of our high resolution model with $r = 60 \cdot \delta_c$ (Fig. 5c) which show focusing of fluid within a narrow channel at the top of the porosity anomaly allows to estimate the growth rate of the porosity increase within the channel. If at some early stage $t_0{}'$ of the channel evolution the amplitude is $A_0 = \varphi_{channel} - \varphi_{ambient}$ and the amplitude grows exponentially as $A(t') = A_0 exp(\alpha_0{}'(t' - t_0{}'))$ we can determine $\alpha_0{}'$ by

$$\alpha_0{}' = ln\left(\frac{A}{A_0}\right)/(t - t_0) \tag{36}$$

These experimentally determined $\alpha_0{}'$ range between 0.5 and 0.72 with a mean of 0.60, which is larger than the analytical $\alpha_0{}'$ derived from equ. (35) by a factor of about 7. We explain this higher experimental growth rate by a) circular geometry, according to which the central channel grows faster than any other channels. Actually, in Fig. 5c this is visible: beside the central channel two weak side lobes appear, and it can be conjectured that the main channel has grown faster by about a factor 3 on the expense of these side channels. b) In Stevenson's (1989) analysis buoyancy has not been included. In our case the fluid

within the channel rises and accumulates in the upper part. If we would redistribute that fluid along the whole channel, the amplitude $A(t)$ would be smaller, perhaps by a factor 2. Altogether, taking these two effects into account, the agreement between the observed growth of the channeling instability and the analytical growth rate can be regarded as reasonably good. This justifies our interpretation of these channels resulting from this instability and being roughly resolved when the grid size is of the order of the compaction length.

4.2. Application to nature

While in our models the perturbation size in terms of compaction lengths was systematically varied but kept constant within in each model, our results might also be applicable to natural cases in which the compaction length varies vertically. In the case of compaction length decreasing with ascent a porosity anomaly might start rising as a solitary wave but then passes through the transition towards diapiric rise. In this case the solitary wave would most certainly enter the regime 2 characterized by strong focusing or channeling followed by a bigger perturbation. A decreasing compaction length could be accomplished by decreasing the matrix viscosity or the permeability, or by increasing the fluid viscosity. Decreasing matrix viscosity might be for example explainable by local heterogeneities, temperature anomalies for example due to secondary convective overturns in the asthenosphere or by a vertical gradient of water content, which may be the result of melt segregation aided volatile enrichment at shallow depths in magmatic systems. This could lead to the propagation of magma-filled cracks (Rubin, 1995) as already pointed out in Connolly & Podladchikov (1998). The latter authors have looked at the effects of rheology on compaction-driven fluid flow and came to similar results for an upward weakening scenario. But this upward weakening might not be strong enough to lead to the focusing needed for the nucleation of dykes. The decrease of permeability due to decrease in background porosity might be an alternative explanation. In the hypothetic case of a porosity wave reaching the top of a magma chamber, the background porosity might decrease which would most certainly lead to focusing, because the compaction length will decrease, and eventually, when reaching melt free rocks, the melt rich fingers may stall as in our models at $r > 50 \cdot \delta_c$ and the rising melt will accumulate and enter the pure diapirism regime. But if the focusing is strong enough and the fluid pressure high enough this scenario could alternatively be a good explanation for the nucleation of dykes. Indeed, if the initiation of dyking is induced by melt channeling instabilities (Stevenson, 1989), our models constrain the minimum size for focused melt anomalies, namely a few compaction lengths. As discussed above, for a partially molten region subject to horizontal extensive stresses Stevenson (1989) determined the growth rate of a channeling instability and found that it reaches a flat maximum plateau for wavelengths smaller than the order of the compaction length. Thus, at the top of our porous diapirs the conditions for melt channeling and subsequent dyking may well be met. As discussed above due to limited resolution in our models we are not able to test this combination of diapiric rise and subsequent channeling on the sub-compaction length scale, however, our resolution test (Fig. 5) is a strong indication for this mechanism.

4.3. Other issues

The introduced partition coefficients help distinguish between a solitary wave and diapirism but there is more information needed, i.e. the matrix and fluid velocity, to really distinguish between the three regimes. For some cases focusing into solitary waves or channels can be observed despite diapirism being dominant. Not until the segregation velocity becomes slower than the matrix, pure diapirism can be observed. These regimes might be not directly applicable to different models e.g. with different amplitudes, rheology laws, permeability laws or background porosities, but their well-defined existence shows that they should exist in generality and the models shown here give an order of magnitude for which perturbation to compaction length ratios one needs to be careful.

The used equation for the Stokes velocity is valid for a sphere and not an infinite long cylinder like the initial perturbation in our 2D model. But still, the velocities fit quite nicely to the observed model velocities. There is no analytic solution for an infinite long cylinder in an infinite medium, but only the solution of a cylinder inside a cylinder with finite radius, where the ratio of both cylinders has some influence on the velocity. For the size of the initial cylindrical wave in a lager cylinder of characteristic size of our model box this solution is nearly identical to the solution of a sphere and therefore it doesn't make sense to use the mathematically more complex solution of a cylinder.

5 Conclusion

This work shows that, depending on the extent of a partially molten region within the earth, the resulting ascent of melt may not only occur by solitary waves or by diapirs, but by an intermediate new mechanism which we call "porosity wave or diapir induced melt focusing and channeling". Depending on the ratio of the melt anomalies size to the compaction length, quantitatively we can classify the ascent behavior into three different regimes using mass flux and velocity of matrix and melt: (1) Solitary wave a and b, (2) porosity wave or diapir induced melt focusing and channeling and (3) diapirism. In regime 1a the matrix sinks with respect to the rising melt, in 1b also the matrix rises, but very slowly. On first order these regimes can be explained by comparing Stokes velocity of the rising perturbation with the solitary waves phase velocity. If the Stokes velocity is higher a diapir will evolve, if lower, a solitary wave will evolve. But even if the Stokes velocity is higher, melt channeling instabilities might be able to focus melt locally within the rising diapiric plume into a frontal channel. These focused channels have a scale of the order of a few compaction lengths. Not until the segregation velocity becomes smaller than the matrix velocity, solitary waves are no longer able to evolve.

Especially in the second regime numerical resolution plays an important role as the compaction length might be no longer resolved properly. Hence it should be generally important for two-phase flow models to inspect the size of partially molten areas with respect to the compaction length, to decide whether possible solitary waves or channeling instabilities are resolved or not.

Code availability

The used finite difference code, FDCON, is available on request.

Author Contribution

Janik Dohmen wrote this article and carried out all models shown here. Harro Schmeling helped preparing this article and had the idea for this project.

References

Barcilon, V., & Lovera, O. M.: Solitary waves in magma dynamics. *Journal of Fluid Mechanics*, *204*(1989), 121–133. https://doi.org/10.1017/S0022112089001680, 1989.

Bittner, D., & Schmeling, H.: Numerical modelling of melting processes and induced diapirism in the lower crust. *Geophysical Journal International*, *123*(1), 59-70, 1995.

Connolly, J. A. D.: Devolatilization-generated fluid pressure and deformation-propagated fluid flow during prograde regional metamorphism. *Journal of Geophysical Research: Solid Earth*, *102*(B8), 18149-18173, 1997.

Connolly, J. A. D., & Podladchikov, Y. Y.: Compaction-driven fluid flow in viscoelastic rock. *Geodinamica Acta*, *11*(2–3), 55–84. https://doi.org/10.1080/09853111.1998.11105311, 1998.

Connolly, J. A. D., & Podladchikov, Y. Y.: A hydromechanical model for lower crustal fluid flow. In *Metasomatism and the chemical transformation of rock* (pp. 599-658). Springer, Berlin, Heidelberg, 2013.

Connolly, J. A. D., & Podladchikov, Y. Y.: An analytical solution for solitary porosity waves: Dynamic permeability and fluidization of nonlinear viscous and viscoplastic rock. *Geofluids*, *15*(1–2), 269–292. https://doi.org/10.1111/gfl.12110, 2015.

Dohmen, J., Schmeling, H., & Kruse, J. P.: The effect of effective rock viscosity on 2-D magmatic porosity waves. *Solid Earth*, *10*(6), 2103-2113, 2019.

Golabek, G. J., Schmeling, H., & Tackley, P. J. (2008). Earth's core formation aided by flow channelling instabilities induced by iron diapirs. *Earth and Planetary Science Letters*, *271*(1-4), 24-33.

Griffiths, R. W.: The differing effects of compositional and thermal buoyancies on the evolution of mantle diapirs. *Physics of the earth and planetary interiors*, *43*(4), 261-273, 1986.

Jordan, J. S., Hesse, M. A., & Rudge, J. F.: On mass transport in porosity waves. *Earth and Planetary Science Letters*, *485*, 65–78. https://doi.org/10.1016/j.epsl.2017.12.024, 2018.

McKenzie, D.: The generation and compaction of partially molten rock. *Journal of Petrology*, *25*(3), 713–765. https://doi.org/10.1093/petrology/25.3.713, 1984.

Omlin, S., Malvoisin, B., & Podladchikov, Y. Y.: Pore Fluid Extraction by Reactive Solitary Waves in 3-D. *Geophysical Research Letters*, *44*(18), 9267–9275. https://doi.org/10.1002/2017GL074293, 2017.

Richard, G. C., Kanjilal, S., & Schmeling, H. (2012). Solitary-waves in geophysical two-phase viscous media: A semi-analytical solution. *Physics of the Earth and Planetary Interiors*, *198–199*, 61–66. https://doi.org/10.1016/j.pepi.2012.03.001

Richardson, C. N.: Melt flow in a variable viscosity matrix. *Geophysical Research Letters*, *25*(7), 1099-1102, 1998.

Rubin, A. M.: Propagation of magma-filled cracks. *Annual Review of Earth and Planetary Sciences*, 287–336, 1995.

Schmeling, H.: Partial melting and melt segregation in a convecting mantle. In *Physics and Chemistry of Partially Molten Rocks*. Springer, 2000.

Schmeling, H., Marquart, G., Weinberg, R., & Wallner, H.: Modelling melting and melt segregation by two-phase flow: New insights into the dynamics of magmatic systems in the continental crust. *Geophysical Journal International*, *217*(1), 422–450. https://doi.org/10.1093/gji/ggz029, 2019.

Scott, D. R.: The competition between percolation and circulation in a deformable porous medium. *Journal Of Geophysical Research*, *93*(B6), 6451–6462. https://doi.org/10.1029/JB093iB06p06451, 1988

Scott, D. R., & Stevenson, D. J.: Magma solitons. *Geophysical Research Letters*, *11*(11), 1161–1164, 1984.

Simpson, G., & Spiegelman, M.: Solitary wave benchmarks in magma dynamics. *Journal of Scientific Computing*, *49*(3), 268–290. https://doi.org/10.1007/s10915-011-9461-y, 2011.

Spiegelman, M.: Physics of Melt Extraction: Theory, Implications and Applications. *Philosophical Transactions of the Royal Society A: Mathematical, Physical and Engineering Sciences*, *342*(1663), 23–41. https://doi.org/10.1098/rsta.1993.0002, 1993.

Spiegelman, M.: Flow in deformable porous media. Part 2 Numerical analysis - the relationship between shock waves and solitary waves. *J. Fluid Mech.*, *247*, 39–63. https://doi.org/10.1017/S0022112093000370, 1993.

Spiegelman, M., & McKenzie, D.: Simple 2-D models for melt extraction at mid-ocean ridges and island arcs. *Earth and Planetary Science Letters*, *83*(1-4), 137-152, 1987.

Šrámek, O., Ricard, Y., & Bercovici, D.: Simultaneous melting and compaction in deformable two-phase media. *Geophysical Journal International*, *168*(3), 964–982. https://doi.org/10.1111/j.1365-246X.2006.03269.x, 2007.

Stevenson, D. J.: Spontaneous small-scale melt segregation in partial melts undergoing deformation. *Geophysical Research Letters*, *16*(9), 1067-1070, 1989.

Turcotte, D. L., & Schubert, G.,. *Geodynamics*. Cambridge university press., 1982.

Watson, S., & Spiegelman, M.: Geochemical Effects of Magmatic Solitary Waves—I. Numerical Results. *Geophysical Journal International*, *117*(2), 284–295. https://doi.org/10.1111/j.1365-246X.1994.tb03932.x, 1994.

Wiggins, C., & Spiegelman, M.: Magma migration and magmatic solitary waves in 3D. *Geophysical Research Letters*, *22*(10), 1289–1292. https://doi.org/10.1029/95GL00269, 1995.

Collins, W. J.: Polydiapirism of the Archean Mount Edgar Batholith, Pilbara Block, Western Australia. *Precambrian Research*, *43*(1-2), 41-62, 1989.

Yarushina, V. M., Podladchikov, Y. Y., & Connolly, J. A. D.: (De)compaction waves in porous viscoelastoplastic media: Solitary porosity waves. *Journal of Geophysical Research: Solid Earth*, 1–20. https://doi.org/10.1002/2014JB011260.Received, 2015.

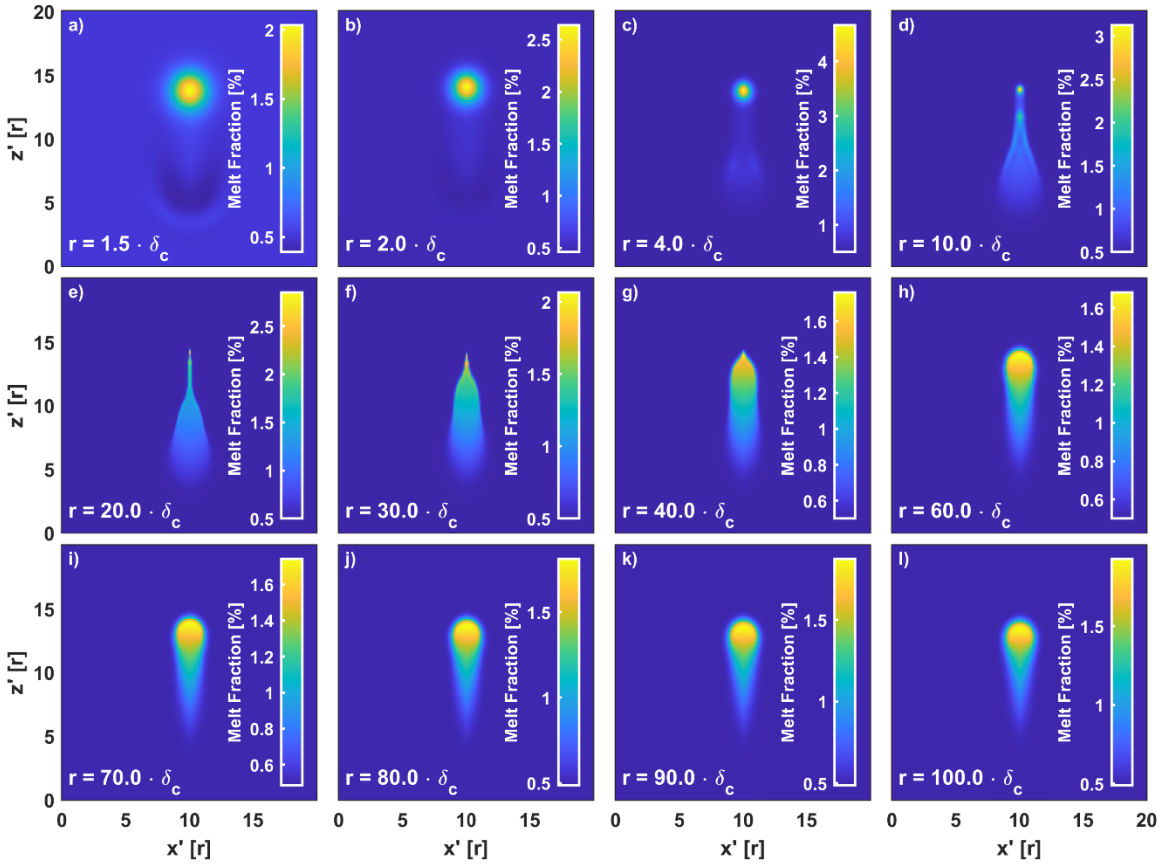

Fig. 1: Resulting melt fraction fields after the maximum melt fraction in the model has reached 70% of the boxes height for different initial perturbation sizes. The surface color gives the melt fraction in percent. The initial perturbation radius of the model is given in white in terms of compaction lengths.

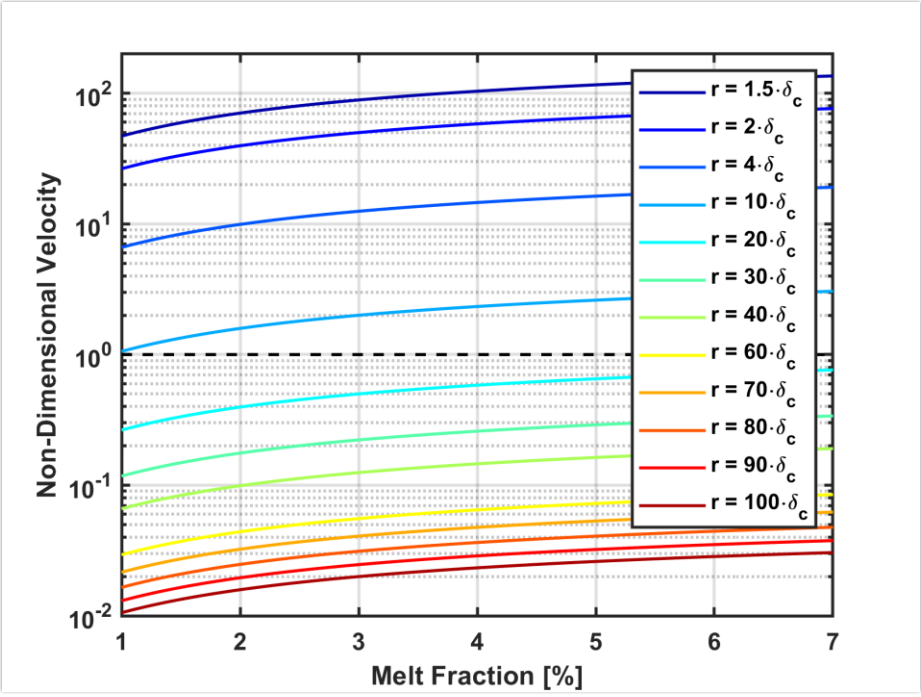

Fig. 2: The dashed line marks the velocity of the Stokes sphere ($v' = 1$). The colored lines show the velocity of a 2D solitary wave, calculated semi-analytically by Simpson & Spiegelman (2011), in our non-dimensionalization, based on the radii shown in the legend.

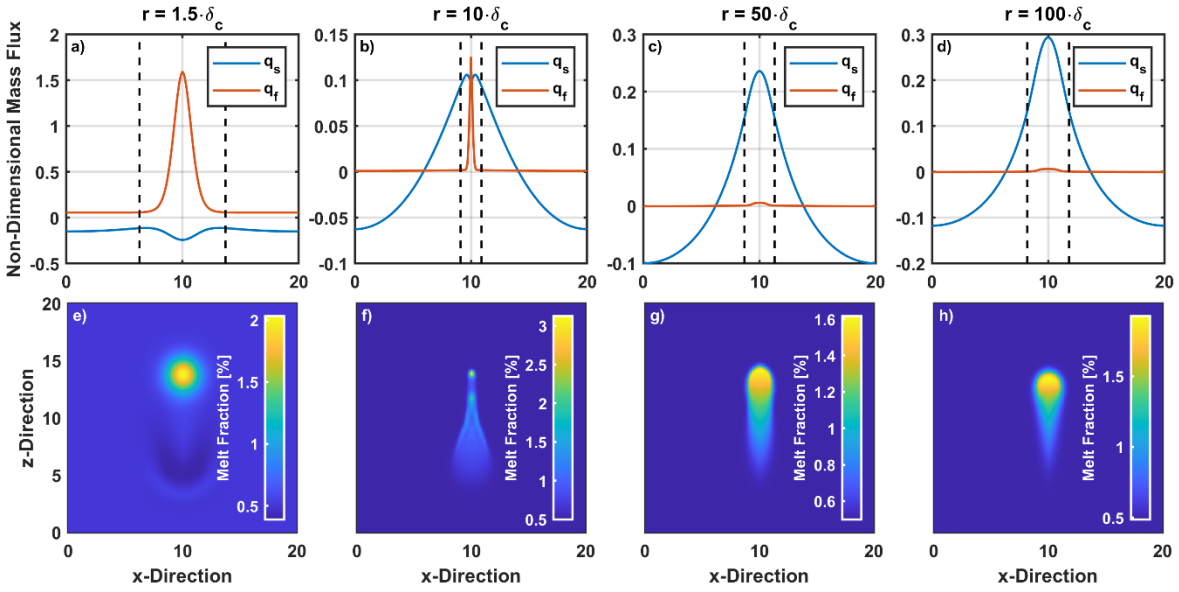

Fig. 3: The upper row gives the solid and fluid mass fluxes of a horizontal line cutting through the maximum melt fraction of the model after it has reached 70% of the models height for different initial perturbation radii. The bottom row gives the corresponding melt porosity fields. All quantities shown are non-dimensional.

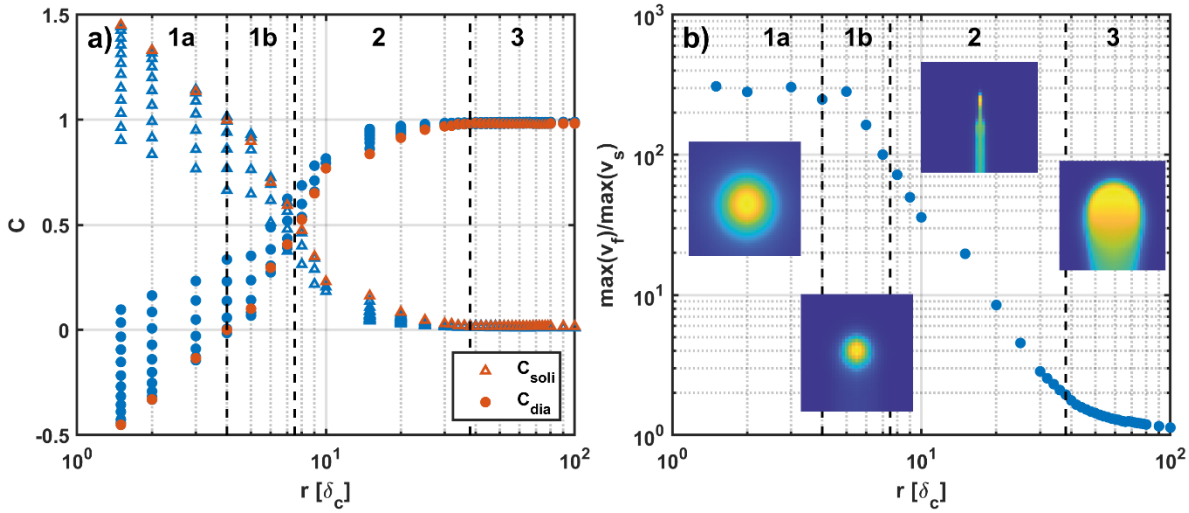

Fig. 4: a) The graph shows the solitary wave and diapir partition coefficients for several initial perturbation radii. The red marker gives the coefficients calculated on a horizontal line at the height of maximum melt fraction. All blue dots give the coefficients calculated at all grid points below the maximum melt fraction as long as at these horizontal lines maximum melt fraction is higher than half the model's maximum. The dashed lines are the borders of the regimes. Figure b) shows the ratio of maximum fluid velocity to maximum solid velocity in the whole model. The

small pictures show typical melt fraction perturbations for each regime. The pictures are from models with an initial perturbation radius of 2, 6, 20 and 60 times the compaction length from left to right.

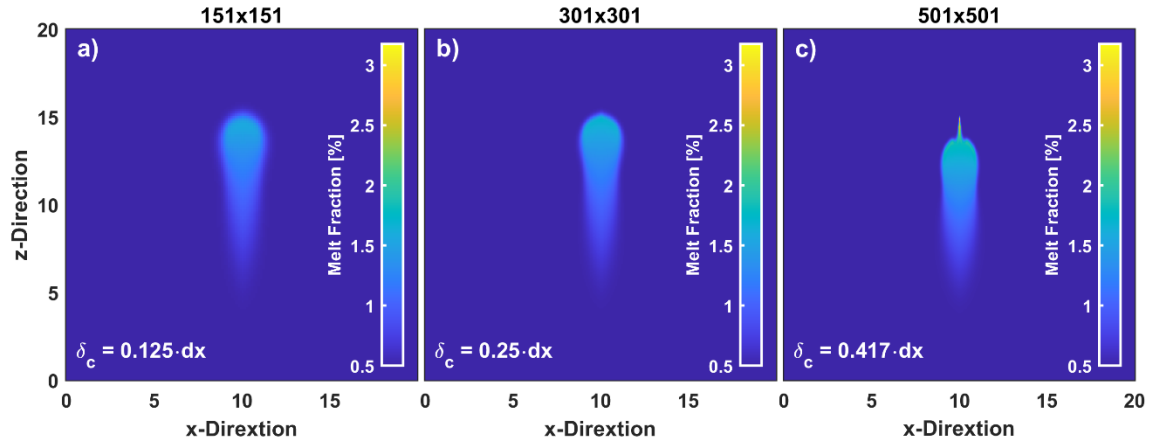

Fig. 5: All three figures show a model with an initial perturbation radius of 60 times the compaction length but with different resolutions: a) 151x151, b) 301x301, c) 501x501. In the lower left corner in each figure the size of the compaction length in terms of grid length is given.